Effect of the latitudinal distribution of temperature at the coronal base on the interplanetary magnetic field configuration and the solar wind flow

Bo Li, Shadia Rifai Habbal,[1] and Xing Li
Institute of Mathematical and Physical Sciences, University of Wales Aberystwyth, Aberystwyth, UK

Chris Mountford
Department of Computer Science, University of York, York, UK

Received 22 July 2005; revised 13 September 2005; accepted 26 October 2005; published 30 December 2005.

[1] Using a two-dimensional MHD model of the corona and solar wind, we investigate the role of the temperature distribution with latitude at the coronal base on the global magnetic field configuration and solar wind properties at 1 AU. The latitudinal distribution of temperature is aimed at modeling the transition in electron temperature at the Sun from a polar coronal hole to the quiet Sun to active regions. The results of the model calculations illustrate how the variation of temperature with latitude impacts the coronal magnetic field configuration and the distribution of wave energy flux in the solar wind and consequently its thermodynamic properties. The sharp temperature changes at the coronal base lead to the formation of current sheets in the corona. They also modify the location of the streamer cusp and the neutral line originating there. Two different approaches in treating electron heat flux are also compared, one assumes a Spitzer expression throughout the computational domain and the other assumes a collisionless expression beyond some radial distance. Model results thus derived differ little in terms of proton flux and terminal speed.

Citation: Li, B., S. R. Habbal, X. Li, and C. Mountford (2005), Effect of the latitudinal distribution of temperature at the coronal base on the interplanetary magnetic field configuration and the solar wind flow, *J. Geophys. Res.*, *110*, A12112, doi:10.1029/2005JA011332.

1. Introduction

[2] The large-scale structure of the solar corona is determined by the interaction between the magnetic field and the coronal plasma. Among these two factors, remote sensing is providing an increasing amount of knowledge about the physical parameters concerning the plasma; however the coronal magnetic field is still among the long standing mysteries in solar physics, mainly because of the difficulties associated with its direct measurement (however, see *Lin et al.* [2004]). Various approaches have been proposed to circumvent the difficulty; among these, multidimensional Magnetohydrodynamic (MHD) modeling has proven useful to relate in situ measurements in interplanetary space to those derived from remote sensing of the inner corona. The coronal magnetic field is inferred once a reasonable match between the model output and the observations is achieved. Owing to the complicated spatial dependence of the measured parameters, three-dimensional (3-D) MHD models are ultimately desired for a detailed comparison between models and observations to be made, as have been pioneered by *Usmanov* [1993] and *Linker et al.* [1999]. Fortunately, we are granted the possibility to assume azimuthal symmetry which is more or less true for the solar corona at solar minimum conditions.

[3] A simplistic picture for the corona at solar minimum consists of a dome-shaped streamer base, presumably the closed magnetic field region, and the overlying equatorial current sheet where the magnetic polarity reverses. Outside the streamer base, the magnetic field lines channel the solar wind. On the basis of this picture a number of 2-D MHD models have been developed, which can roughly be categorized into two groups. The first one employs the iterative approach, first proposed by *Pneuman and Kopp* [1971], which has been extended by various authors [*Yeh and Pneuman*, 1977; *Robertson*, 1983; *Stewart and Bravo*, 1997; *Vásquez et al.*, 2003]. More modeling efforts seem in favor of the second approach, the time-relation one. Initiated by *Endler* [1971] and *Steinolfson et al.* [1982], this approach advances the MHD equations toward a steady state from the perspective of initial-boundary value problem. As such, the final quasi-steady state will bear no ambiguity concerning its stability [*Washimi et al.*, 1987] which has sometimes been an issue with the iterative

[1] Also at Institute for Astronomy, University of Hawaii, Honolulu, Hawaii, USA.

0148-0227/05/2005JA011332$09.00

approach. However, an ensuing question is that whether the system will eventually reach a steady state in the presence of a cusp point in the strict sense. So far this has not been well established mathematically, although recent results by *Hu et al.* [2003a] do suggest the existence of a unique steady state.

[4] Recent advances based on the latter approach have been directed at incorporating physical ingredients like field-aligned conductive flux, the energy and momentum exchange between different species or the same species but in different degrees of freedom, ad hoc or explicitly specified heating and/or momentum addition [*Wang et al.*, 1993, 1998; *Ofman and Davila*, 1997, 1998; *Davila and Ofman*, 1999; *Suess et al.*, 1999b; *Usmanov et al.*, 2000; *Chen and Hu*, 2001; *Usmanov and Goldstein*, 2003; *Hu et al.*, 2003a, 2003b; *Ofman*, 2004; *Li et al.*, 2004] or the radiative loss when the transition region is taken into account [*Lionello et al.*, 2001]. Other natural applications include the study of the long-term behavior of the solar corona and the solar wind in response to the injection of large-amplitude Alfvén waves [*Grappin et al.*, 2002, 2003] or the uniform heating applied to the inner corona and the consequent insufficient energy loss to the transition region [*Endeve et al.*, 2003, 2004].

[5] Whatever approach is adopted, specification of the lower boundary is of vital importance in determining the final steady state. At that boundary, the characteristic theory requires that the number of dependent variables that can be arbitrarily specified should not exceed the number of incoming characteristics (from the boundary into the computational domain). The rest has to be determined in the form of compatibility relations, usually expressed in terms of variation of base values with time. However, in practice, a combination of simple means like fixing base temperature, upward mass flux [*Keppens and Goedbloed*, 2000] or density [e.g., *Lionello et al.*, 2001] seems to work as well as those from compatibility relations [*Wang et al.*, 1993, 1998]. The lower boundary is not necessarily identified with the coronal base. In fact, a number of studies place this boundary at some level in the upper transition region [*Keppens and Goedbloed*, 2000] or the top of the chromosphere [*Lionello et al.*, 2001]. Since the pressure of the transition region should adjust to the inward heat flux from the corona, the latter treatment could suffer further complication in specifying the base conditions, even though simple means seem to work fine.

[6] Observations of the solar disk show that plasma conditions at the coronal base can by no means be uniform. The simplest distribution at solar minimum implies a latitude-dependent distribution of thermodynamical parameters such as density or temperature. Some of these considerations have been taken into account in the two-dimensional model of *Hu et al.* [2003a] where the magnetic flux and density distribution with latitude were prescribed, albeit with a uniform base temperature in the open magnetic field region.

[7] It is the intent of this paper to study the effect of the latitudinal distribution of base temperature on the solar wind flow. Experience from 1-D computations suggests that the terminal mass flux is sensitive to the base temperature (T_b); more specifically, a modest increase in base temperature could result in a significant increase in mass flux at 1 AU. However, missing from such studies is the understanding of how changes of base temperature are translated into changes of coronal magnetic field intensity with a subsequent signature at 1 AU.

[8] In what follows, the governing equations along with the boundary conditions will be described in section 2, section 3 will present model results with different base temperature distributions, and a summary and some concluding remarks will be given in section 4.

2. Model Description

2.1. Governing Equations

[9] Assuming azimuthal symmetry in spherical geometry (r, θ, ϕ) allows the magnetic field $\mathbf{B}$ to be expressed in terms of the magnetic flux function $\psi(r, \theta, t)$, i.e.,

$$\mathbf{B} = \nabla\psi \times \frac{\hat{\phi}}{r\sin\theta}, \tag{1}$$

in which $\hat{\phi}$ is the unit vector along the azimuthal direction. The time-dependent equations describing an electron-proton solar wind plasma are given by

$$\frac{\partial\rho}{\partial t} + \mathbf{v}\cdot\nabla\rho + \rho\nabla\cdot\mathbf{v} = 0, \tag{2}$$

$$\frac{\partial\mathbf{v}}{\partial t} + \mathbf{v}\cdot\nabla\mathbf{v} + \frac{1}{\rho}\nabla\left(p_e + p_p + p_w\right) + \frac{1}{4\pi\rho}\mathcal{L}\psi\nabla\psi + \frac{GM_S}{r^2}\hat{\mathbf{r}} = 0, \tag{3}$$

$$\frac{\partial\psi}{\partial t} + \mathbf{v}\cdot\nabla\psi = 0, \tag{4}$$

$$\frac{\partial T_e}{\partial t} + \mathbf{v}\cdot\nabla T_e + (\gamma-1)T_e\nabla\cdot\mathbf{v} + 2\nu_{pe}\left(T_e - T_p\right) + \frac{\gamma-1}{nk_B}\nabla\cdot\mathbf{q}_e = 0, \tag{5}$$

$$\frac{\partial T_p}{\partial t} + \mathbf{v}\cdot\nabla T_p + (\gamma-1)T_p(\nabla\cdot\mathbf{v}) + 2\nu_{pe}\left(T_p - T_e\right) - \frac{\gamma-1}{nk_B}Q_p = 0, \tag{6}$$

$$\frac{\partial p_w}{\partial t} + \nabla\cdot\left[\left(\frac{3}{2}\mathbf{v} + \mathbf{v}_\mathbf{A}\right)p_w\right] - \frac{\mathbf{v}}{2}\cdot\nabla p_w + \frac{Q_p}{2} = 0, \tag{7}$$

where

$$\mathcal{L}\psi = \frac{1}{r^2\sin\theta}\left(\frac{\partial^2\psi}{\partial r^2} + \frac{1}{r^2}\frac{\partial^2\psi}{\partial\theta^2} - \frac{\cot\theta}{r^2}\frac{\partial\psi}{\partial\theta}\right).$$

Quasi-neutrality and zero current have been assumed so that $n_e = n_p = n$ and $\mathbf{v}_e = \mathbf{v}_p = \mathbf{v}$ where n is the plasma number density and $\mathbf{v}$ denotes the bulk flow velocity. The proton mass is m_p, and $\rho = nm_p$ is the plasma mass density. The

Boltzmann constant is k_B, G is the gravitational constant, and M_S the solar mass. The electron and proton pressure are given by $p_e = nk_BT_e$ and $p_p = nk_BT_p$, where T_e and T_p denote electron and proton temperature. Here $\gamma = 5/3$ is the adiabatic index. Alfvén waves are taken to be the only external source in driving and heating the solar wind. The proton heating Q_p due to Alfvénic turbulence is given by the Kolmogorov rate [*Hollweg*, 1986]

$$Q_p = \frac{2^{3/2} p_w^{3/2}}{\rho^{1/2} L_c}, \tag{8}$$

where p_w is the wave pressure and L_c is the dissipation length and will be given in subsequent section. Moreover, $\mathbf{v}_A = \mathbf{B}/\sqrt{4\pi\rho}$ is the Alfvén speed.

[10] The collision frequency ν_{pe} is [*Braginskii*, 1965]

$$\nu_{pe} = \frac{4\sqrt{2\pi m_e} n e^4 \ln\Lambda}{3 m_p k_B^{3/2} T_e^{3/2}}, \tag{9}$$

where m_e and e are the mass and electric charge of electrons, ln Λ is the Coulomb logarithm, chosen to be 23 in the calculations. The electron heat flux density $\mathbf{q}_e$ is supposed to be collision-dominated, namely,

$$\mathbf{q}_e = -\kappa_0 T_e^{5/2} \hat{\mathbf{b}}\hat{\mathbf{b}} \cdot \nabla T_e \tag{10}$$

is used, where $\hat{\mathbf{b}}$ is the unit vector along the background magnetic field, $\kappa_0 = 7.8 \times 10^{-7}$ erg $\cdot$ K$^{-7/2} \cdot$ cm$^{-1} \cdot$ s^{-1} is the electron conductivity [*Spitzer*, 1962]. The electron heat flux across the magnetic field, as well as the proton heat flux are neglected.

[11] The electron conductive flux $\mathbf{q}_e$ probably can not be well approximated by the Spitzer form, especially in the dilute fast wind. An alternative approach has been suggested by *Hollweg* [1974] (see also *Hollweg* [1978]) to account for the possible collisionless behavior of the electron gas. We will examine in section 3.5 to what extent the two approaches differ, as far as the bulk speed and mass flux are concerned.

2.2. Boundary Conditions

[12] The pole ($\theta = 0°$) and the equator ($\theta = 90°$) are assumed to be symmetrical boundaries. At the top boundary (placed at $r = 258R_S$), linear extrapolation is applied to each dependent variable for simplicity. All the unknowns at the coronal base are prescribed with the exception of the two components of the flow vector, v_r and v_θ, which are determined through the equivalent extrapolation of mass flux along flow tubes together with the condition $\mathbf{v} \| \mathbf{B}$.

[13] Following *Hu et al.* [2003a], the magnetic flux carried by the open magnetic field (0°, 60°) is set equal to the closed flux underlying the helmet streamer. Furthermore, the open flux emerging from (0°, 30°) is set equal to that from (30°, 60°). The magnetic flux ψ_b can thus be described by the following relations:

$$\psi_b = \begin{cases} \frac{1-\cos^9\theta}{2\left[1-\left(\sqrt{3}/2\right)^9\right]}\psi_c, & 0° \le \theta \le 30°, \\ \frac{\sqrt{3}-\cos\theta-0.5}{\sqrt{3}-1}\psi_c, & 30° \le \theta \le 60°, \\ 2\left(2\sin^2\theta - 1\right)\psi_c, & 60° \le \theta \le 90°, \end{cases} \tag{11}$$

with $\psi_c = 7.4 \times 10^{21}$ Mx, corresponding to an average radial magnetic field of 3.3 γ at the Earth orbit $R_E = 215R_S$. In deriving equation (11), the radial magnetic field B_r is supposed to scale as $\cos^8\theta$ for $\theta \le 30°$ in accordance with observations of coronal holes [*Svalgaard et al.*, 1978] but is constant for $30° \le \theta \le 60°$. Magnetically, the two regions can be recognized as coronal hole and open field regions other than the coronal hole. The latter will be our test bed to impose various temperature distributions.

[14] The density at the coronal base is chosen to be

$$n_b = \begin{cases} 1.5 \times 10^8 (\cos\theta)^{-1} \mathrm{cm}^{-3}, & 0° \le \theta \le 60° \\ 3 \times 10^8 \mathrm{cm}^{-3}, & 60° \le \theta \le 90°. \end{cases} \tag{12}$$

The Alfvén wave pressure at the coronal base is

$$p_{w,b} = \begin{cases} \frac{p_{wp}}{\sqrt{\cos\theta}}[1 + 0.02\theta(f_2 - 1)], & 0° \le \theta \le 50° \\ \frac{p_{wp}}{\sqrt{\cos\theta}}[f_1 + 0.1(60 - \theta)(f_2 - f_1)], & 50° \le \theta \le 60° \\ 0, & 60° \le \theta \le 90°, \end{cases} \tag{13}$$

where $f_2 = 1.25$, $f_1 = 0.7$. Wave pressure at the pole is $p_{wp} = n_p m_p \langle \delta v_p^2 \rangle / 2$, and n_p and $\langle \delta v_p^2 \rangle^{1/2}$ refer to the number density and the Alfvénic turbulent velocity amplitude at the solar pole. In this study, we choose $\langle \delta v_p^2 \rangle^{1/2} = 30$ km/s. The Alfvén wave dissipation length in equation (8) is

$$L_c = \begin{cases} \left(B_p/B\right)^{1/2}\left[1 + 1.6(\psi/\psi_c)^{3/2}\right] L_{c0}, & 0 \le \frac{\psi}{\psi_c} \le 0.8, \\ \left(B_p/B\right)^{1/2} L_{c0}, & 0.8 \le \frac{\psi}{\psi_c} \le 1 \end{cases} \tag{14}$$

with B_p being the magnetic field strength at the solar pole; L_{c0} is set to be 3.9×10^4 km. Moreover, the wave pressure p_w is set to zero where the magnetic field is closed; hence there is no additional energy input to the base of the helmet streamer. The description of coronal base temperature specification is left to section 3.

3. Numerical Results

[15] To explore the impact on the solar wind of the electron temperature distribution with latitude, as supported by coronal observations [e.g., *Habbal et al.*, 1993], we present a series of solar wind models corresponding to different distributions of base temperature T_b with latitude, as described in Table 1. A reference model, namely case D of *Hu et al.* [2003a], is designated case 1 in Table 1.

[16] From case 1 to case 3, the temperature jump is moved away from the streamer boundary ($\theta = 60°$) toward the coronal hole boundary ($\theta = 30°$). In case 4, T_b varies linearly with θ, while in cases 5 and 6, a stepwise distribution of T_b is implemented.

[17] With this choice of base temperatures, equations (2) to (7) are solved using the multistep implicit scheme of *Hu et al.* [2003a]. In practice, the computational domain [1,258] $R_S \times [0°, 90°]$ is discretized into a 180 $\times$ 60 mesh. The radial grid spacing Δr increases from $0.02R_S$ at $1R_S$ to $0.72R_S$ at $12.2R_S$ and remains so until $30R_S$, after which Δr increases steadily to $3.92R_S$ at $164R_S$ and is kept constant thereafter. As for the latitudinal grid spacing, $\Delta\theta$ decreases by a constant ratio from 4° at the pole to 1° at 60°,

Table 1. Specification of the Base Temperature Distribution

Case	T_b specification
Case 1	$T_b = \begin{cases} 1\text{MK}, & 0 \le \theta \le 60^\circ \\ 2\text{MK}, & 60 \le \theta \le 90^\circ \end{cases}$
Case 2	$T_b = \begin{cases} 1\text{MK}, & 0 \le \theta \le 45^\circ \\ 2\text{MK}, & 45 \le \theta \le 90^\circ \end{cases}$
Case 3	$T_b = \begin{cases} 1\text{MK}, & 0 \le \theta \le 30^\circ \\ 2\text{MK}, & 30 \le \theta \le 90^\circ \end{cases}$
Case 4	$T_b = \begin{cases} 1\text{MK}, & 0 \le \theta \le 30^\circ \\ \frac{\theta}{30}\text{MK}, & 30 \le \theta \le 60^\circ \\ 2\text{MK}, & 0 \le \theta \le 30^\circ. \end{cases}$
Case 5	$T_b = \begin{cases} 1\text{MK}, & 0 \le \theta \le 30^\circ \\ 1.3\text{MK}, & 30 \le \theta \le 60^\circ. \\ 2\text{MK}, & 60 \le \theta \le 90^\circ \end{cases}$
Case 6	$T_b = \begin{cases} 1\text{MK}, & 0 \le \theta \le 30^\circ \\ 1.6\text{MK}, & 30 \le \theta \le 60^\circ \\ 2\text{MK}, & 60 \le \theta \le 90^\circ \end{cases}$

remaining constant thereafter. Starting with an arbitrary initial state, a steady state for case 1 can be established after a physical time of 300 hours. Using this solution as the initial state (physical time $t = 0$), we then alter the base temperature distribution to the desired one and run the code until a steady state is reached. To establish such a state, it takes considerably more time in cases 2 and 3 where we take the solution at the physical time $t = 1000$ hours as the steady state. It is relatively faster to reach the desired solution for cases 4–6, in which we employ the solution at $t = 500$ hours.

[18] In what follows, we will first compare case 1 with case 2 in order to gain insight into what happens when we introduce the assumed temperature distribution. This comparison will facilitate the analysis for case 3, where the temperature jump is moved further from the streamer base, and cases 5 and 6, where two temperature jumps are introduced. Meanwhile, the analysis of case 4 will illustrate the effect of a continuous temperature distribution.

3.1. Cases 1 and 2: Effect of a Single Temperature Jump

[19] A comparison of the latitudinal distribution at 1 AU of (a) speed v, (b)flux nv and (c)electron (T_e) and proton temperatures (T_p), and (d) magnetic field strength for case 1 (solid line) and case 2 (dashed line) is given in Figure 1. In that figure, the vertical line designates the latitude at 1 AU of the flux tube originating from $\theta_b = 45^\circ$ in case 2. Therefore the solar wind in the regions separated by the vertical bar has different base temperatures. The reference model (case 1) reproduces the standard correlation between flow speed v, mass flux nv, and proton temperature T_p. In that model, a knee-point appears at 73°, below which the wind speed is larger than 700 km/s, with little variation with θ in the wind speed v, the particle flux nv, and the temper-

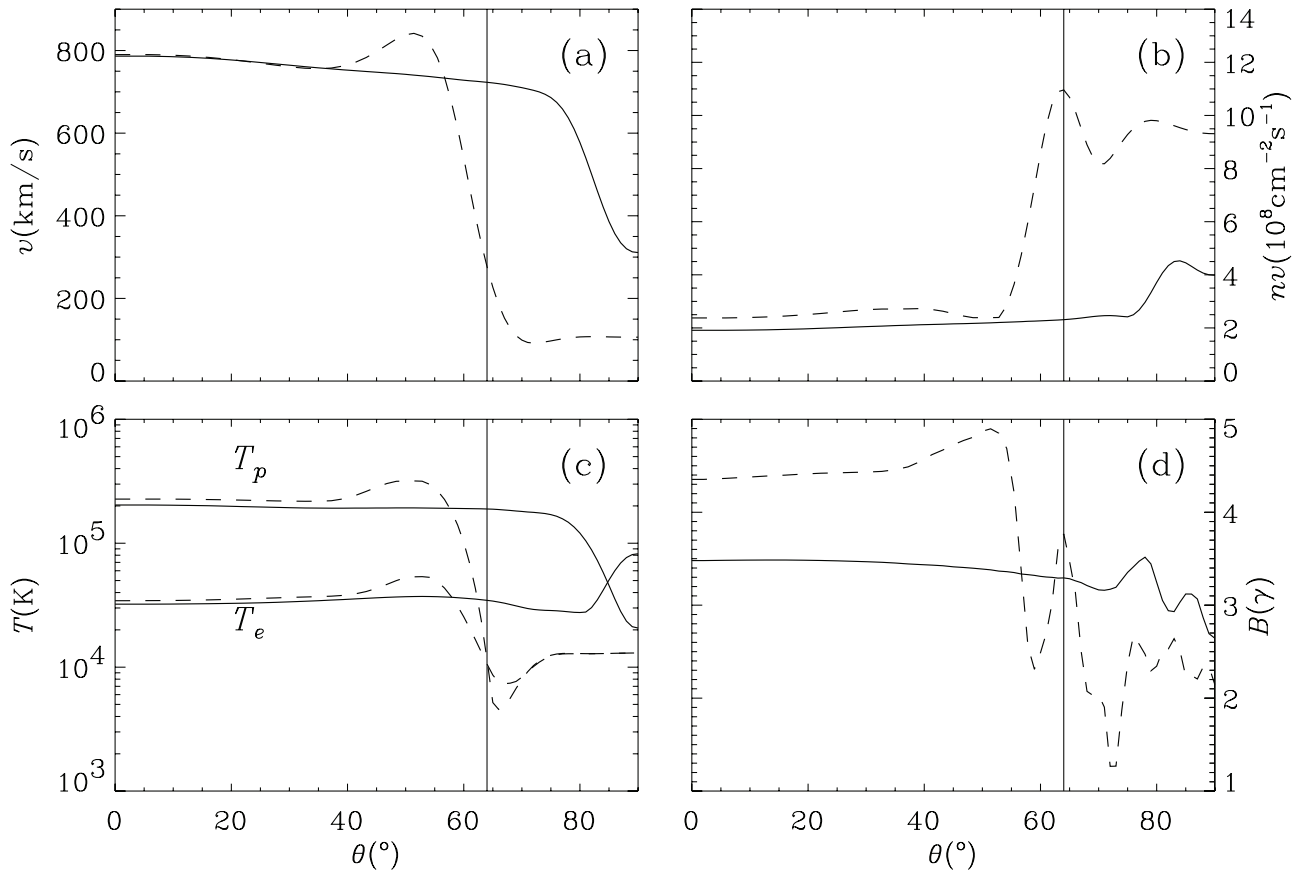

Figure 1. The latitudinal distribution at 1 AU of (a) flow speed v, (b) particle flux nv, (c) electron T_e and proton T_p temperature, and (d) magnetic field strength B for case 1 (solid line) and case 2 (dashed line). The vertical line gives the location of the flux tube $\psi(r = 1R_S, \theta = 45^\circ)$ at 1 AU for case 2.

atures T_e, T_p. Beyond the knee-point, the wind speed v decreases sharply toward the equator and so does the proton temperature T_p. Detailed discussions of the reference model, including a comparison between the model output and Ulysses measurements, have been given by *Hu et al.* [2003a] and will not be presented further in this paper. Now comparing cases 1 and 2, one can see a band of extremely slow and dense wind in the region $\theta > 70°$, where the flow speed is around 100 km/s. Taking the flow at the equator $\theta = 90°$ for instance, the flow is by assumption channeled by the flux tubes bordering the streamer base, which in case 1 has a base temperature of 1 MK but now corresponds to 2 MK. It is no surprise that the particle flux (in units of 10^8 cm^{-2} s^{-1}) is enhanced from 4 to more than 9.3. It should be noted that in case 2, the wind for $\theta > 87°$ comes from the initially closed field region (see the discussion of Figure 4). For such a dense plasma, Coulomb coupling is efficient enough to keep the electrons and protons nearly in thermodynamic equilibrium $T_e \approx T_p$ as can be seen in Figure 1c.

[20] In case 2, the knee-point is replaced by a relatively narrow transition layer across which the wind speed increases to about 740 km/s at 57°. Then comes a region between 57° and 37° where the flow speed v is enhanced in comparison with case 1. The speed profile exhibits a hump and attains a local maximum of 840 km/s at 51°, which is found to be associated with a local minimum in mass flux. Below 37°, there is no tangible difference in the speed profile between cases 1 and 2; yet, the particle flux nv and proton temperature T_p are both larger in case 2 than in case 1. For instance, the particle flux at the pole (0°) increases from 1.91×10^8 to 2.38×10^8 cm^{-2}.s^{-1}.

[21] It is interesting to consider the energy budget for this fast stream since the energy flux F consists mainly of the kinetic F_k and potential F_p one. Recalling that $F_k \propto nv \cdot v^2$ and $F_p \propto nv$ (cf. equation (16)), there should be an increase in the energy flux F for the fast stream as well. Specifically, F at the pole increases by 25% from 1.6 in case 1 to 1.99 erg cm^{-2} s^{-1} in case 2. Given that the fast stream has a base temperature identical to case 1, this energy deficit turns out to be due to the changes in the magnetic field.

[22] Neglecting the time dependence, equations (2) to (7) can be combined to give a conservation law

$$\nabla \cdot \left[\frac{1}{2} n m_p v^2 \mathbf{v} - \frac{GM_S}{r} n m_p \mathbf{v} + (2\mathbf{v}_A + 3\mathbf{v}) p_w + \frac{\gamma}{\gamma - 1}(p_e + p_p)\mathbf{v} + \mathbf{q}_e\right] = 0, \tag{15}$$

where terms inside the square parentheses are identified with fluxes of kinetic, potential, and wave energy as well as enthalpy and electron conductive flux. Alternatively, equation (15) can be expressed by scaling the energy fluxes to 1 AU, i.e.,

$$\frac{B_E}{B}\left[\frac{1}{2} n m_p v^3 + \frac{GM_S m_p}{R_S}\left(1 - \frac{R_S}{r}\right) nv + (2v_A + 3v) p_w + \frac{\gamma}{\gamma - 1}(p_e + p_p) v + q_e\right] = \text{tube constant}, \tag{16}$$

where B_E denotes the magnetic field strength at Earth orbit.

[23] The latitudinal profile of the magnitude of the magnetic field B at 1 AU, shown in Figure 1d, reveals that the magnetic field is enhanced in the fast stream region for $\theta > 57°$ but decreases in the slow wind region for $\theta > 70°$. Sandwiched between both is a layer where B shows a strong latitudinal dependence. At the pole, the magnetic field has a strength of 3.48γ in case 1 but increases to 4.35γ for case 2.

[24] When scaled to 1 AU, and neglecting the inflow v at the coronal base, the input wave flux in equation (16) becomes $2p_{w,b}B_E/\sqrt{4\pi n_b m_p}$, which is directly proportional to B_E. The wave flux is therefore increased by the same factor relative to its counterpart in case 1. Since for the model solutions, the Alfvén waves virtually exhaust their energy while propagating from the coronal base out to 1 AU, the enhanced magnetic field strength at 1 AU therefore accounts for the increased mass flux for the fast stream for $\theta \leq 57°$. Similarly, the hump in the speed profile in Figure 1a corresponds to a local maximum of energy flux of the flow, which can be explained in view of the enhanced wave flux as evidenced by the hump in the B profile.

[25] Let us move on to the wind beyond 70° in case 2. In general, this band of wind has a larger energy flux compared to that in case 1 due to the much larger mass flux. Taking that at 90° for example, the total energy flux is 3.0 erg cm^{-2} s^{-1} at 1 AU in case 2, almost twice as much as that in case 1. The wave flux input for the band of slow wind plays a less significant role as the electron conductive flux, q_e which scales as $T_e^{5/2}$, and the enthalpy flux at the base, which scales as $T_e + T_p$ act as the main driving mechanism. Between 57° and 70°, a strong velocity shear can be seen. Strongly sheared flow is well known to be susceptible to Kelvin-Helmholtz (K-H) instability [e.g., *Chandrasekhar*, 1961]. The resolution of the present numerical solution is unfortunately too limited for a detailed investigation to be made, and we shall not pursue it any further.

[26] The evolution with heliocentric distance of the latitudinal profile of the magnetic field strength B, is given in Figure 2, where the continuous and dashed lines represent cases 1 and 2, respectively. The location of the flux tube rooted at 45° at the base in case 2, are given by vertical lines in each panel for different radial distances. Both cases display a similar redistribution of magnetic flux to relax the latitudinal gradient of B below $10R_S$. Only beyond $4R_S$ does a perceptible difference appear at high latitudes. Beyond $10R_S$, case 1 shows little variation in the latitudinal dependence of B, indicating little redistribution of the magnetic flux. In contrast, the magnetic field profile in case 2 is considerably changed, giving rise to an equatorward gradient for $\theta < 52°$ as well as irregular features elsewhere.

[27] Inspection of the location of the vertical line shows that below $10R_S$, the flux tube rooted at 45° in case 2 bends over toward the equator with increasing radial distance. For instance, the locus of the flux tube moves to 65° at $4R_S$ and shows little variation between $4R_S$ and $10R_S$ at which distance the locus of the flux tube is at 67°. Beyond $10R_S$, the flux tube shows a slight poleward migration reaching 64° at 1 AU.

[28] The electric current **J** does not appear in equations (2) to (7), in this sense it serves as a secondary variable. An alternate view would be that **J** is the source term as given

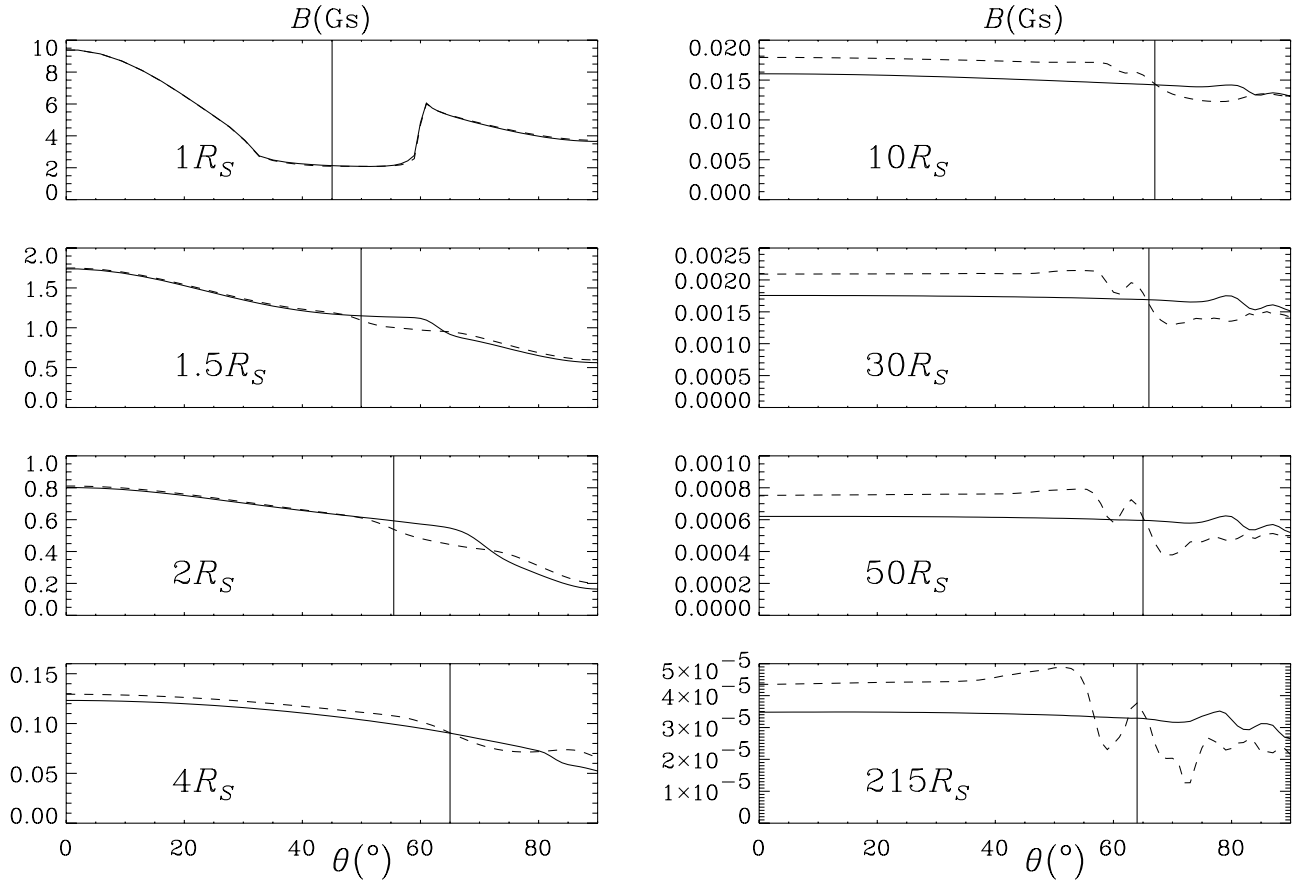

Figure 2. The latitudinal distribution of magnetic field strength B at different radial distances as labeled. The vertical bar in each panel gives the location of the flux tube originating from $\theta_b = 45°$ in case 2.

by the magnetic induction equation, i.e., $\nabla \times \mathbf{B} = 4\pi\mathbf{J}/c$. Therefore the changes in the magnetic field can be attributed to changes in the distribution of electric current $\mathbf{J}$, which becomes $\mathbf{J} = J\,\hat{\phi}$ for 2D computations. Figure 3 gives the global distribution of J for case 1 (Figure 3a) and case 2 (Figure 3b). For case 1, there are two major electric current concentrations: the separatrix which borders the magnetically closed region, and the equatorial current sheet overlying the streamer base. The current density J around the streamer base peaks at 0.34 statamp cm^{-2} at the coronal base and gradually decreases with radial distance. The existence of such a current concentration is a well-known effect, arising from the fact that the plasma flow bordering the streamer base decreases the pressure scale height, resulting in a thermal pressure imbalance between closed and open magnetic field regions. Since the pressure imbalance has to be compensated by the magnetic pressure, an electric current concentration appears.

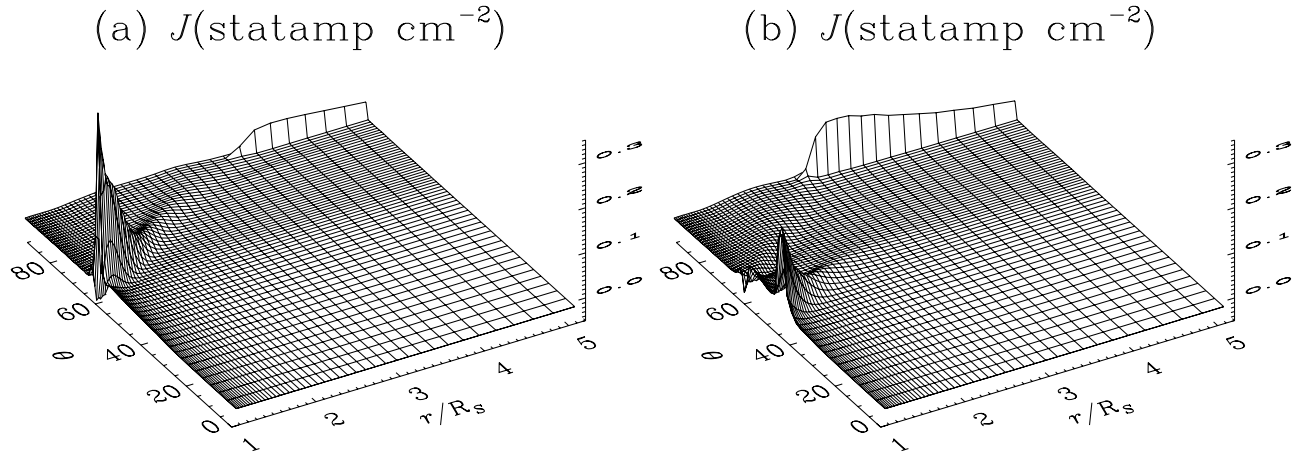

Figure 3. Surface plot of electric current density J for (a) case 1 and (b) case 2.

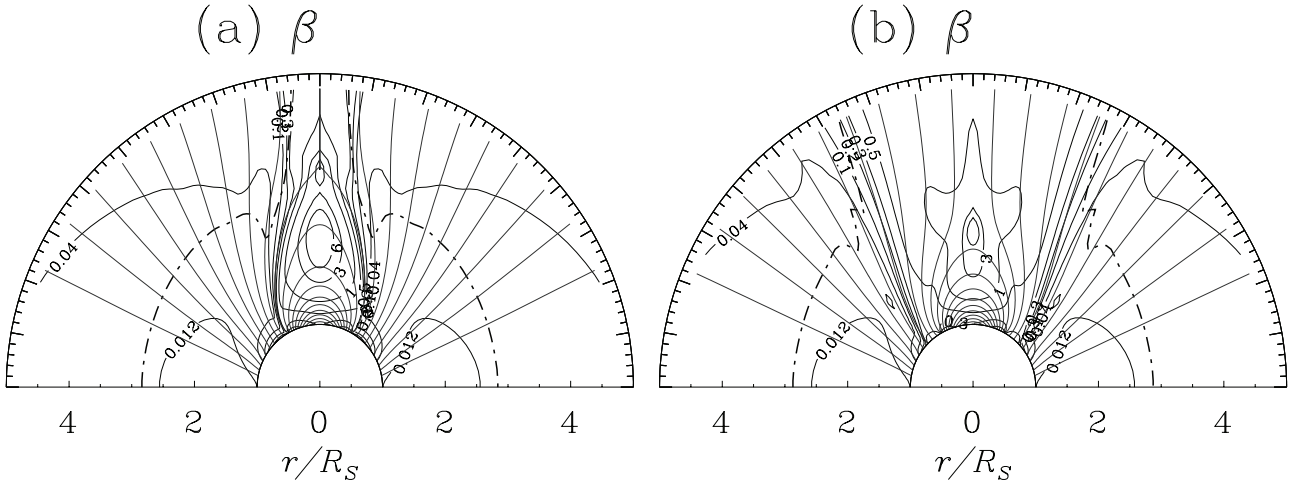

Figure 4. The contour of $\beta = 8\pi(p_e + p_p + p_w)/B^2$, which takes into account the contribution of wave pressure, for (a) case 1 and (b) case 2. The thick dash-dotted line is the sonic critical curve where the sonic Mach number equals one. The magnetic field configuration is given by the light contours of ψ, which are equally spaced by $0.1\psi_c$, ψ_c being the open flux initially assumed.

[29] The location of the cusp point can be identified with the point beyond which J shows an abrupt increase, from nearly zero at the cusp point located at $3.52R_S$, to 0.052 statamp cm^{-2} at $3.9R_S$, and decreasing gradually thereafter to 0.035 statamp cm^{-2} at $5R_S$. For case 2, apart from the equatorial current sheet, the current density is more intensely concentrated in the narrow layer originating from the imposed temperature jump at the coronal base. This current attains its maximum of 0.17 statamp cm^{-2} at the coronal base. The current along the streamer border is less intense and does not exhibit a perceptible sheet. Also obvious is that the cusp point moves inwards to $2.5R_S$, when compared to $3.52R_S$ in case 1. The equatorial current is stronger than that in case 1, reaching a maximum of 0.12 statamp cm^{-2} at $2.9R_S$ before declining with distance.

[30] It is useful to consider the transverse force balance, which can be obtained by taking the cross product of equation (3) with **B** (note that the Lorentz force term in its most general form is $\frac{1}{c}\mathbf{J} \times \mathbf{B}$), [cf. *Pneuman and Kopp*, 1971]

$$J = -\frac{1}{B}\left[\frac{\partial}{\partial \mathcal{N}}(p_T) + \frac{GM_S m_p}{r^2} n \sin\delta + \frac{n m_p v^2}{\mathcal{R}}\right], \qquad (17)$$

where $p_T = p_e + p_p + p_w$ is the total pressure, $\mathcal{N}$ denotes the direction normal to the magnetic field, $\mathcal{R}$ the curvature radius, δ the angle between the magnetic field and the radial direction. In view of this, the fact that the streamer border current concentration is less prominent in case 2 can be attributed to the significantly reduced pressure imbalance across the streamer boundary.

[31] Figure 4 shows the contour of plasma $\beta = 8\pi p_T/B^2$, superimposed on the magnetic field configuration, equally spaced by $0.1\psi_c$. Also plotted is the sonic critical curve $M = 1$ (thick dash-dotted line), where the Mach number is $M = v/v_s$ with $v_s = \sqrt{p_T/\rho}$. It can be seen that in case 1, the plasma β is well below unity outside the helmet; however, in the bulk of the helmet, β is larger than 1, which reinforces the notion that a realistic streamer is maintained magnetically by the ambient magnetic field [*Suess et al.*, 1999a]. However, in case 2, the plasma β is of order unity in the regions surrounding the streamer base. As a consequence, the streamer is not as well contained as in case 1 and is gradually stripped of the magnetic flux by the outflowing plasma, as evidenced by the contour for $\psi = \psi_c$ which in Figure 4a is right at the equator but now off the equator in Figure 4b. In other words, part of the slow wind that reaches 1 AU, $\theta > 87°$ in case 2, comes from the regions that are gradually opened during relaxation. The continual loss of the magnetic flux can in part account for the shrinkage of the streamer base, which is more obviously shown in Figure 4b.

[32] This process has been discussed by *Suess et al.* [1996] who suggest that eventually the whole helmet will disappear, the magnetic flux being fully opened into the interplanetary space. In our computation, however, the timescale associated with the gradual stripping of magnetic flux is too long to be a valid means to explain the ultimate disappearance of the streamer. During a time interval of 1000 hours (or 42 days), the magnetic flux lost by the streamer base is only about 0.073 ψ_c based on the data set between $t = 600$ and 1600 hours. This loss rate shows no sign of acceleration with elapsing time. Recall that in the model assumptions, the magnetic flux contained in the helmet is initially ψ_c, which results in an estimate of 575 days for the helmet to become fully open. Volumetric heat deposition inside the closed field region should be able to expedite the process [*Suess et al.*, 1996] but further investigation into this subject is beyond the scope of the present study.

[33] Across the streamer boundary β undergoes a steep transition in case 1, reflecting the steep gradient in both the total pressure p_T and the magnetic field B. For case 2, the steep transition in β is seen to occur across the magnetic field line separating regions having different base temperatures. On the contrary, β has only a modest gradient in the direction normal to the streamer border, reflecting only a weak imbalance in p_T or B. This can also be understood

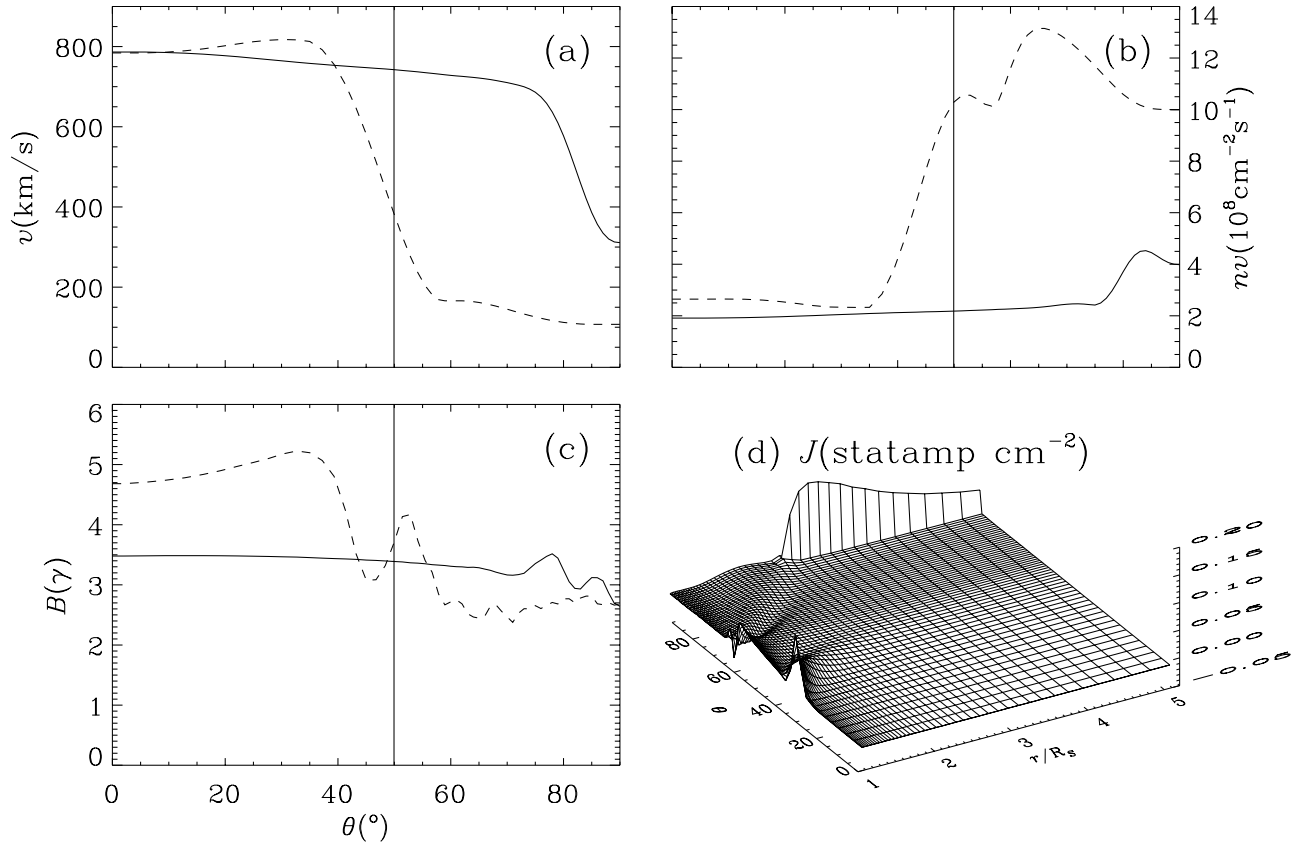

Figure 5. Latitudinal distribution at 1 AU of (a) flow speed v, (b) flux nv and (c) magnetic field strength B for case 1 (solid lines) and case 3 (dashed). The vertical line gives the location of the flux tube for $\psi = \psi(r = 1R_S, \theta = 30°)$ at 1 AU in case 3. (d) The surface plot of electric current density J in the inner corona for case 3.

from the different profiles of the acoustic curve M = 1. The plasma is less accelerated along the streamer border in case 2, as evidenced by the much more protruded shape of the sonic critical curve. Projecting equation (3) on the magnetic field **B** results in

$$\frac{\partial}{\partial s}\left(p_T + \rho v^2\right) - \rho v^2 \frac{\partial}{\partial s} \ln B + \rho \frac{GM_S}{r^2} \cos\delta = 0. \qquad (18)$$

Since M measures the relative importance of kinetic to thermal pressure ($M^2 = \rho v^2/p_T$), it is no wonder that the kinetic pressure arising from the slow flow only produces a minor thermal pressure imbalance across the streamer border.

3.2. Case 3: Moving the Temperature Jump Further Away From the Base of the Streamer

[34] With the experience gained in understanding case 2, we can now readily examine case 3, where the temperature jump is moved to 30° at the coronal base. Figure 5 displays the latitudinal profile at 1 AU of the flow speed v (Figure 5a), flux nv (Figure 5b), and magnetic field strength B (Figure 5c). Solid lines are used to plot case 1, whereas dashed ones are for case 3. For ease of analysis, the vertical line in each panel gives the locus of the flux tube rooted at 30°. Similar to case 2, an enhanced flow region is now shifted to the interval [13°, 40°]. Below 13°, the flow speed is effectively unchanged but the flux is increased. The relative change (a factor of 35% at 0°) in the magnetic field strength is larger than that in case 2 relative to case 1 (25% at 0°), sufficient to explain the energy budget necessary to drive a more energetic fast wind. The flow speed decreases steeply from 755 km/s at 40° to 166 km/s at 58°. For $\theta > 58°$ the solar wind shows little variation in flow speed but an appreciable one in flux. Between 40° and 60° the relatively intense variation in magnetic field implies a relatively strong electric current there. The electric current J (Figure 5d) shows a concentration at the separatrix anchored at 30° where the temperature jump is imposed. At the coronal base, J peaks at 0.11 statamp cm^{-2} at 30°. The cusp point now is located at about $2.5R_S$, beyond which J increases to 0.14 statamp cm^{-2} at $2.8R_S$ before declining with radial distance.

3.3. Case 4: Effect of a Continuous Temperature Structure

[35] The effect of a continuous temperature structure imposed at the coronal base is shown in Figure 6, where the latitudinal distribution of flow speed (Figure 6a), flux nv (Figure 6b), and magnetic field B (Figure 6c) of case 4 (dashed line) is compared to case 1 (solid line). The vertical line gives the locus of the flux tube rooted at 30° for case 4. For the wind originating from a base temperature of 1 MK (to the left of the vertical bar), when compared with case 1,

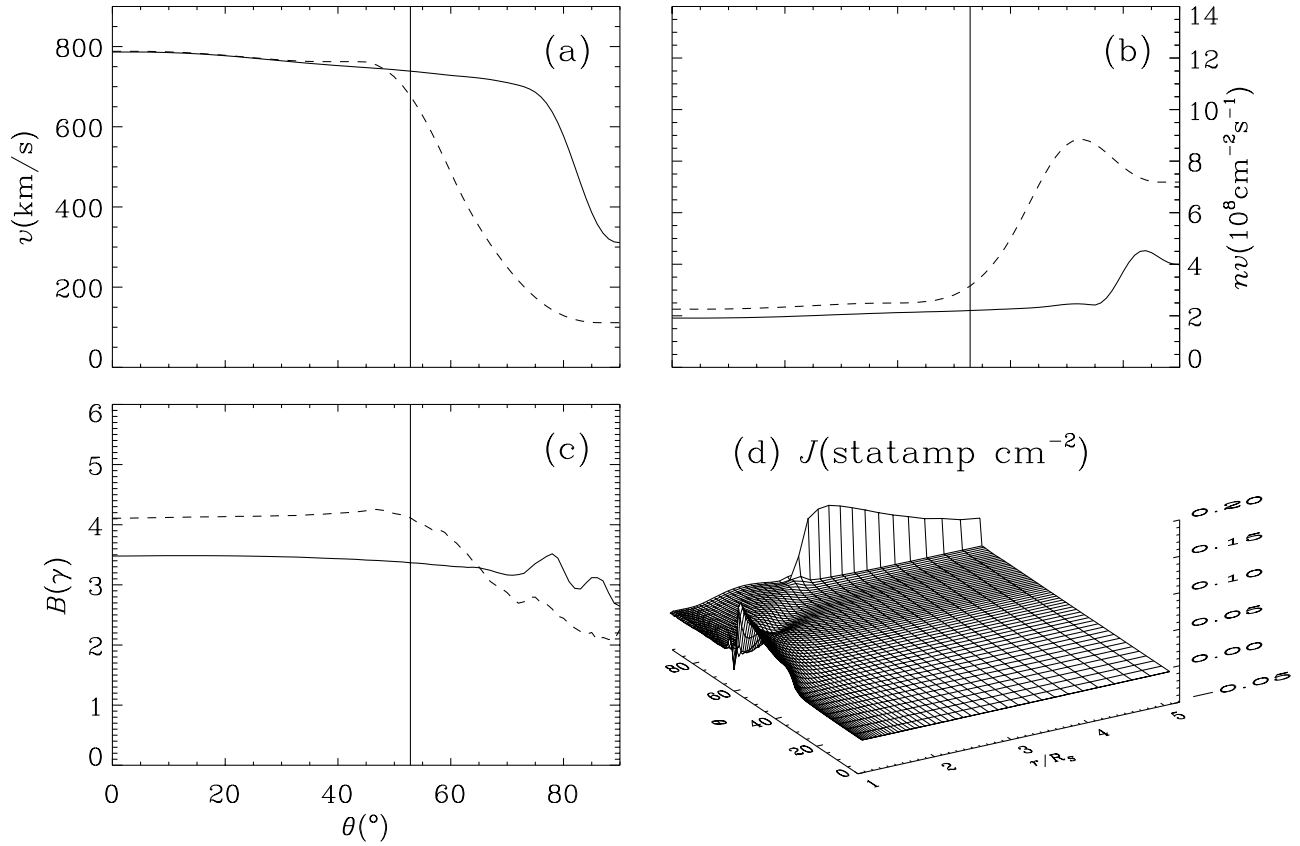

Figure 6. Latitudinal distribution at 1 AU of (a) flow speed v, (b) flux nv and (c) magnetic field strength B for case 1 (solid lines) and case 4 (dashed). The vertical line describes the locus of the flux tube rooted at 30° for case 4. (d) The surface plot of electric current density J in the inner corona for case 4.

case 4 shows little difference in speed v and a modest difference in flux nv. The magnetic field shows an increase of 18% at 0° relative to case 1. For $\theta > 53°$, the flow speed in case 4 decreases steadily from 677 km/s to 112 km/s at 90°. The magnetic field profile shows a similar latitudinal dependence.

[36] Figure 6d describes the spatial dependence of electric current density J for case 4 below $5R_S$. Below the cusp point, now located at $2.8R_S$, J does not show apparent concentration but is rather diffusely distributed outside the streamer base. Taking the coronal base for example, J shows a steady increase from 0.01 at 30° to 0.08 statamp cm^{-2} at 57°. As for the equatorial current sheet, J peaks at 0.1 statamp cm^{-2} at $3.1R_S$ beyond which J declines gradually with heliocentric radius to 0.037 statamp cm^{-2} at $5R_S$.

3.4. Cases 5 and 6: Effect of Introducing Two Temperature Jumps

[37] Since by assumption the solar wind flows out of open field regions only, among the two introduced temperature jumps at the coronal base, only that located at the coronal hole border ($\theta = 30°$) will directly show up in the solar wind solution. (The magnetic flux stripping is very limited in both cases 5 and 6. In case 6, only the fraction $\theta > 88.6°$ is from the initially closed region, while in case 5 this fraction is even smaller.) The one located at the streamer border will mainly contribute to the electric current distribution and thus the magnetic field configuration. Similar to case 2 or 3, there also exhibit slightly enhanced flux and flow speed in the fast stream, understandable in light of the enhanced magnetic field, which has been discussed earlier.

[38] Figure 7 gives the spatial distribution of the electric current density J in the inner corona for cases 5 and 6. The magnitude of the temperature jumps can be seen to determine the relative intensity of the current concentration, the stronger the transverse gradient in p_T, the stronger the intensity of J (cf. equation (17)). For instance, the peak of the current (in statamp cm^{-2}) surrounding the streamer base is about 0.25 at 59° for case 5 but only 0.15 at the same position for case 6. In the same fashion, the peak of the current at 30° is about 0.039 for case 5 but 0.07 for case 6. In case 5, the cusp point is located at $3.35R_S$, above which J peaks at 0.056 at $3.7R_S$. The cusp in case 6 is at $2.9R_S$ and J possesses a local maximum of 0.078 at $3.35R_S$. Hence the cusp point moves closer to the Sun as the temperature at the base increases.

3.5. An Alternative Treatment of Electron Conductive Flux $\mathbf{q}_e$

[39] All the model computations presented above assume the classical Spitzer expression for the electron conductive flux $\mathbf{q}_e$. With the increasing heliocentric distance, the solar wind electrons could gradually become collisionless as the plasma becomes increasingly dilute. As such, it may seem questionable to use a uniform expression throughout the computational domain. To tackle this problem, *Hollweg*

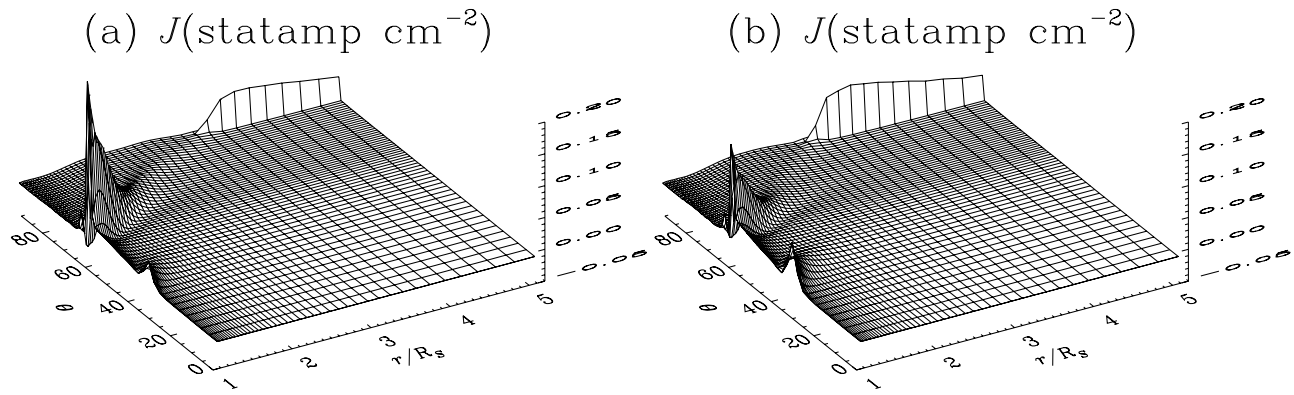

Figure 7. The spatial distribution of electric current density J in the inner corona for (a) case 5 and (b) case 6.

[1974] has proposed an approach where the computational domain is divided into two regions characterized by different treatment of $\mathbf{q}_e$. In the inner region, the Spitzer expression is employed, whereas in the outer one, an expression for $\mathbf{q}_e$ is proposed to account for its collisionless nature, namely,

$$\mathbf{q}_H = \frac{3}{2}\alpha n k_B T_e \mathbf{v}, \tag{19}$$

where α is of order unity. The interface of both regions is taken to be where the electron mean free path λ_e is comparable to the characteristic spatial scale in question, where

$$\lambda_e = v_{th,e}/\nu_{ee}, \tag{20}$$

with $v_{th,e}$ being the electron thermal speed and ν_{ee} the electron self-collision frequency. Such a treatment has been accommodated in many numerical studies, among which are some two-dimensional ones by, e.g., *Lionello et al.* [2001], *Endeve et al.* [2003, 2004], and *Ofman* [2004]. To our knowledge, no direct comparison between model results from both treatments has been reported. It therefore seems informative to present such a comparison to assess to what extent different treatments for $\mathbf{q}_e$ impacts the solar wind flow.

[40] A simple way to implement such a treatment is to assume

$$\mathbf{q}_e = \eta \mathbf{q}_S + (1-\eta)\mathbf{q}_H, \tag{21}$$

where $\mathbf{q}_S$ denotes the Spitzer law (equation (10)), $\mathbf{q}_H$ denotes the Hollweg ansatz (equation (19)) in which $\alpha = 1$ is assumed. Moreover, η describes a smooth transition between both expressions [cf. *Ofman*, 2004]

$$\eta = \frac{1}{2}\left(1 - \tanh\frac{r - r_{coll}}{h_{coll}}\right). \tag{22}$$

[41] Figure 8 displays the latitudinal distribution at 1 AU of (a) flow speed v, (b) proton flux nv, (c) the temperatures of electrons T_e and protons T_p, and (d) the magnetic field strength B. The model results given in solid lines are for Case 1 where the Spitzer law is used (or equivalently $r_{coll} = \infty$), whereas model results in dashed lines assume $r_{coll} = 6R_S$ and $h_{coll} = 0.5R_S$ (referred to as Case 1q). Most notable differences appear, not surprisingly, in the electron temperature profile (Figure 8c) for the region $\theta > 60°$. The speed profile v is slightly raised (Figure 8a). Taking into account that at the equator, the proton flux also increases (Figure 8b), the slow wind should be more energetic in Case 1q. This is understandable in light of the enhanced magnetic field strength (Figure 8d), which compensates the lowered thermal pressure.

[42] We however limit ourselves to Case 1 and have not carried out similar comparison for other cases. Such a choice stems from the following considerations. First, the equation (19) is derived from the electron velocity distribution function (VDF) resulting from an exospheric model in which the electrons are assumed to be free of collisions as well as wave-particle interaction. Such an electron VDF is however subject to instabilities, say whistler mode, which lead to the ultimate interaction between the amplified waves and electrons (perhaps also ions) [see *Hollweg*, 1978; *Marsch*, 1991]. Moreover, the electron-electron collision may not be negligible, in not only the slow but also the fast wind. Indeed, the expansion timescale (say $1/|\nabla \cdot \mathbf{v}|$) seems to be larger than the electron-electron collision time throughout [see also *Olsen and Leer*, 1996, Figure 4]. (Note that here the expansion speed v instead of the electron thermal speed $v_{th,e}$ is used). Second, although still desired, the nonlocal treatment for electron heat flux is not without controversy. In the meantime, more researches have been shifted towards the ion dynamics in light of the SOHO discoveries (cf. the extensive review by *Hollweg and Isenberg* [2002]).

4. Concluding Remarks

[43] We explored the effect of the electron temperature distribution with latitude at the base of the corona, representing the observed transition from coronal hole to quiet Sun to active regions, on the global properties of the solar wind. The parameter study is made by using a 2-D solar wind model driven by Alfvén waves initially developed by *Hu et al.* [2003a], therefore complementing their study. It is found that the variation in the temperature distribution

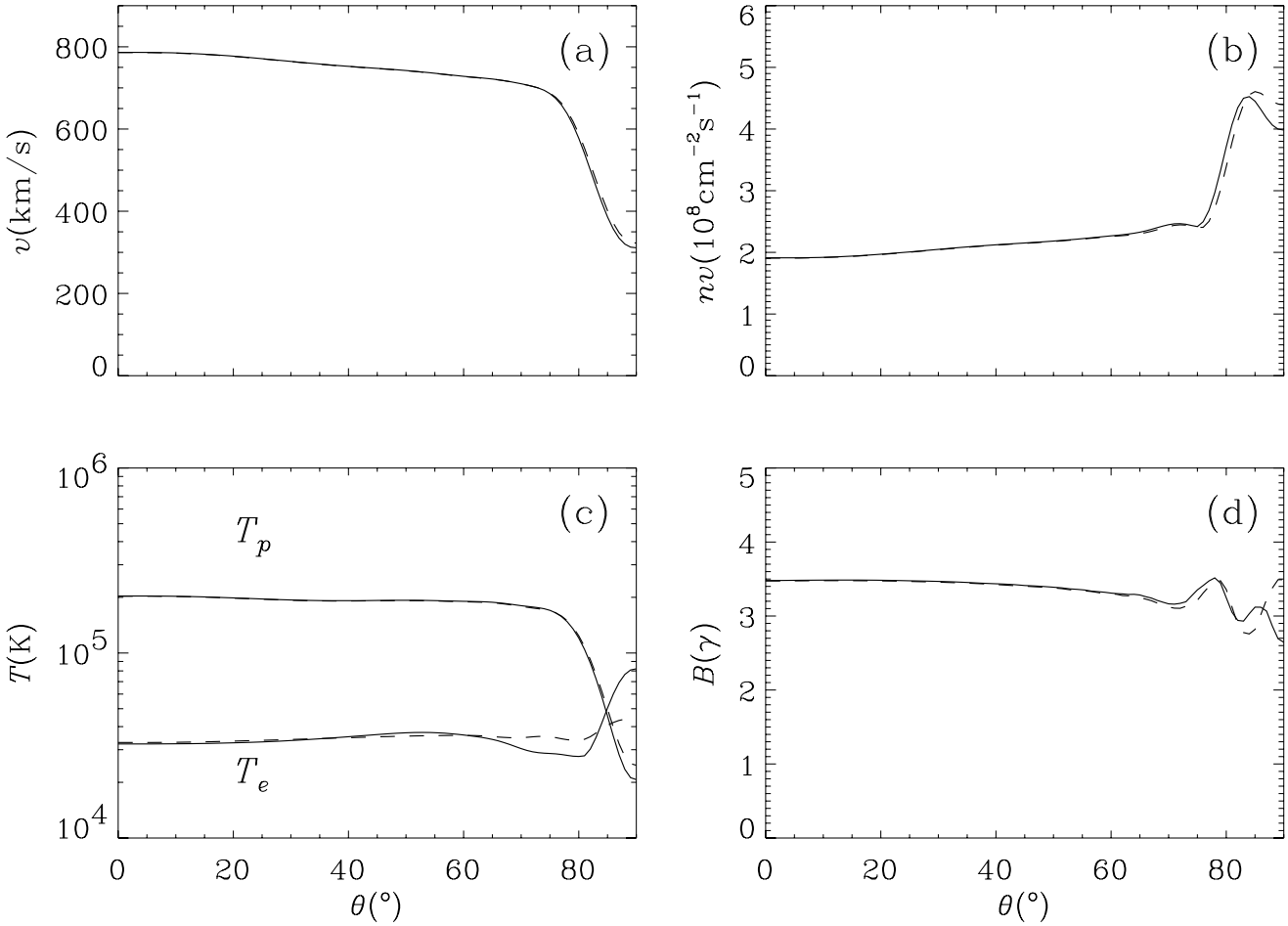

Figure 8. Latitudinal profile at 1 AU of (a) flow speed v, (b) proton flux nv, (c) the temperatures of electrons T_e and protons T_p, and (d) the magnetic field strength B. Solid lines are used to plot Case 1 where the Spitzer law is used, whereas dashed lines depict the model where the electron heat flux is assumed to undergo the transition from the collision-dominated Spitzer law to collisionless Hollweg ansatz.

imposed at the coronal base outside the coronal hole can alter the global distribution of the electric current density and subsequently change the magnetic field distribution. Consequently, the energy deposition from Alfvén waves is modified, thus altering the properties of the fast solar wind originating from the polar coronal hole regions with both enhanced particle flux and flow speed identified at 1 AU. Introducing a sharp temperature change at the base leads to the formation of the electric current concentration, whose intensity depends on the magnitude of the temperature jump. The thermodynamic boundary may substantially influence the magnetic field configuration, as evidenced by different locations of the cusp points. The model results show little difference when the Hollweg ansatz for the electron heat flux is introduced in the outer computational domain, as far as the proton terminal speed and flux are concerned.

[44] The slow stripping of the magnetic flux off the streamer base, facilitated by the thermal boundary condition, needs to be further addressed. To examine whether this is a numerical artefact, we have performed three additional computations using identical parameters as in case 2 but on different grids. As before, we first obtain a reference steady model on the new grid using the boundary conditions in case 1. The steady state is taken as the initial state $t = 0$ for the computation where the boundary condition is adapted to the desired one. The time evolution of the solutions is then examined. Four different grid sets have been tested, the standard one 180 × 60, two coarser ones 140 × 50, 100 × 40, and a finer one 180 × 90. If the spatial resolution is further increased, the computation will be formidably slow. It is found that the flow properties are consistent on all grids, and we shall discuss in what follows the stripping of the magnetic flux only. On the coarser grids, the flux stripping is only present during the interval 500–900 (500–1200) hours for 100 × 40 (140 × 50) grid (after which, the magnetic flux does not vary with time). During that interval, the rate of flux stripping is consistent with that presented in case 2. On the finer grid 180 × 90, however, the stripping persists from $t = 450$ hours on, as is the case on the standard grid. The two grids yield consistent rates of flux stripping. Given these computations, we suggest that

the leakage present in case 2 is very unlikely of pure numerical nature. However, in either case, such a low rate of leakage ($0.07\psi_o$ per 1000 hours) is only of theoretical interest since for a realistic solar atmosphere, the magnetic diffusion should operate on a shorter timescale to disrupt the whole configuration [cf. *Linker and Mikić*, 1995].

[45] The sensitivity of the mass flux at 1 AU to the base temperature, presumed to be that at the coronal base, has long been recognized. In this sense it is not surprising to see the models yield drastically different slow wind when the base temperatures are varied. What is more fascinating is that the changes in some area of the base can also influence the wind properties originating elsewhere, the magnetic field acts as an intermediary between regions that are thermally isolated as implied by the infinite electric conductivity as well as the assumption that the electron conductive flux is field-aligned.

[46] The inner boundary for the solar wind flow, in the models presented here, is assumed to be the base of the corona. The fact that the coronal base can not be unambiguously identified has provoked long-standing conjectures that the problems of coronal heating and solar wind heating/acceleration are intimately related and therefore have to be treated on equal footing [e.g., *Hollweg*, 1986]. The very recent correlation study by *Tu et al.* [2005] between the Doppler-velocity, the radiance map of several ultraviolet (UV) lines and the extrapolated magnetic field calls for the renewal of our understanding of the source region of the solar wind, at least those fast ones in coronal holes: the nascent fast wind is formed at neither the coronal base nor the top of the chromosphere but some point in the magnetic funnel where the downflows change into upflows. As such, the formation of the solar wind is intrinsically 3-D and seems to undermine the highly idealized treatments such as those presented in the present paper. However, the problem of heating and accelerating the nascent wind as it reaches the level where transversal mixing ceases (presumably at the bottom of the transition region) still persists. From the modeling perspective, it therefore becomes more reasonable to set the lower boundary somewhere at the bottom of the transition region and include the magnetic flux variations there to account for the initial expansion of the flow tubes, which can have significant influences on the flow properties [*Li*, 2003]. By doing so, the coronal conditions assumed here will be derived in a more self-consistent fashion. In this regard, the present model can be seen as a first step to elucidate the effects on the global solar wind of those changes in the transition region that are able to give the supposed base distribution of plasma conditions.

[47] Observations have demonstrated that the quiet Sun and the polar coronal hole, although both seem to be permeated with open magnetic flux, can have different temperatures [*Habbal et al.*, 1993]. In view of the fact that the coronal base adjusts its pressure to the inward heat flux from the corona, which is determined by the entire heating process [e.g., *Hansteen and Leer*, 1995], the heating mechanism can be different even in regions with similar magnetic topologies, not to mention regions with different ones as have been demonstrated by *Lionello et al.* [2001]. This has inspired us to implement a computation (Case 2) where the base pressure is very different across $\theta = 45^\circ$ which is located in the open field region. As mentioned above, an ultimate goal for modeling effort should be to derive rather than prescribe coronal base conditions consistent with observations by, say, varying the heating parameters.

[48] The inclusion of part of the transition region in multidimensional MHD models is complex. Nevertheless, advancement towards this direction has been taken by various authors. The model by *Lionello et al.* [2001] treats the problem in spherical coordinates and is able to derive the global structure of the transition region. On the other hand, the model by *Aiouaz et al.* [2004] solves the single-fluid MHD equations in the Cartesian coordinates and can include some low-lying magnetically closed structures. To implement a computation that takes into account the radiative loss in the transition region, retains the two-fluid nature of the solar wind and relates the properties of the transition region to those of the solar wind at 1 AU will provide more insight into the overall understanding of solar wind as well as coronal heating. This is, however, left to the next study which is now underway.

[49] In closing, we note that the pressure imbalance between the closed and open magnetic field region could render the configuration unstable in the presence of the electrical resistivity, as shown by *Endeve et al.* [2003, 2004] where a uniform base heating is applied to facilitate the buildup of such a pressure imbalance. When driven unstable, the streamer base releases periodically plasmoids that can significantly contribute to the mass loss from the Sun. This scenario can be accommodated in the present code, but further pursuit is beyond the scope of the present paper.

[50] **Acknowledgments.** This work was supported by a PPARC rolling grant to the University of Wales Aberystwyth.

[51] Arthur Richmond thanks the reviewers for their assistance in evaluating this paper.

References

Aiouaz, T., H. Peter, and R. Keppens (2004), Forward modeling of coronal funnels, in *SOHO 15 Coronal Heating*, *ESA SP-575*, edited by R. W. Walsh et al., pp. 337–341, Eur. Space Agency, Paris.

Braginskii, S. I. (1965), Transport phenomena in a plasma, in *Reviews of Plasma Physics*, vol. 1, pp. 205, Consultant Bureau, New York.

Chandrasekhar, S. (1961), *Hydrodynamic and Hydromagnetic Stability*, Oxford Univ. Press, New York.

Chen, Y., and Y. Q. Hu (2001), A two-dimensional Alfvén-wave-driven solar wind model, *Sol. Phys.*, *199*, 371–384.

Davila, J. M., and L. Ofman (1999), Two-fluid 2.5D MHD simulations of the fast solar wind in coronal holes and the relation to UVCS observations, *Space Sci. Rev.*, *87*, 165–168.

Endeve, E., E. Leer, and T. E. Holzer (2003), Two-dimensional Magnetohydrodynamic models of the solar corona: Mass loss from the streamer belt, *Astrophys. J.*, *589*, 1040–1053.

Endeve, E., T. E. Holzer, and E. Leer (2004), Helmet streamers gone unstable: Two-fluid Magnetohydrodynamic models of the solar corona, *Astrophys. J.*, *603*, 307–321.

Endler, F. (1971), Interaction between the solar wind and coronal magnetic fields, Ph.D. thesis, Gottingen University, Gottingen, Germany.

Grappin, R., J. Léorat, and S. R. Habbal (2002), Large-amplitude Alfvén waves in open and closed coronal structures: A numerical study, *J. Geophys. Res.*, *107*(A11), 1380, doi:10.1029/2001JA005062.

Grappin, R., J. Léorat, and S. R. Habbal (2003), Large amplitude Alfvén waves in open and closed coronal structures, in *Solar Wind 10*, edited by M. Velli, R. Bruno, and F. Malara, *AIP Conf. Proc.*, *679*, 277–282.

Habbal, S. R., R. Esser, and M. B. Arndt (1993), How reliable are coronal hole temperatures deduced from observations?, *Astrophys. J.*, *413*, 435–444.

Hansteen, V. H., and E. Leer (1995), Coronal heating, densities, and temperatures and solar wind acceleration, *J. Geophys. Res.*, *100*, 21,577–21,594.

Hollweg, J. V. (1974), Electron heat-conduction in solar-wind, *J. Geophys. Res.*, *79*, 3845–3850.

Hollweg, J. V. (1978), Some physical processes in the solar wind, *Rev. Geophys.*, *16*, 689–720.
Hollweg, J. V. (1986), Transition region, corona, and solar wind in coronal holes, *J. Geophys. Res.*, *91*, 4111–4125.
Hollweg, J. V., and P. A. Isenberg (2002), Generation of the fast solar wind: A review with emphasis on the resonant cyclotron interaction, *J. Geophys. Res.*, *107*(A7), 1147, doi:10.1029/2001JA000270.
Hu, Y. Q., S. R. Habbal, Y. Chen, and X. Li (2003a), Are coronal holes the only source of fast solar wind at solar minimum?, *J. Geophys. Res.*, *108*(A10), 1377, doi:10.1029/2002JA009776.
Hu, Y. Q., X. Li, and S. R. Habbal (2003b), A 2.5-dimensional MHD Alfvén-wave-driven solar wind model, *J. Geophys. Res.*, *108*(A10), 1378, doi:10.1029/2003JA009889.
Keppens, R., and J. P. Goedbloed (2000), Stellar winds, dead zones, and coronal mass ejections, *Astrophys. J.*, *530*, 1036–1048.
Li, B., X. Li, Y. Hu, and S. R. Habbal (2004), A two-dimensional Alfvén wave-driven solar wind model with proton temperature anisotropy, *J. Geophys. Res.*, *109*, A07103, doi:10.1029/2003JA010313.
Li, X. (2003), Transition region, coronal heating and the fast solar wind, *Astron. Astrophys.*, *406*, 345–356.
Lin, H., J. R. Kuhn, and R. Coulter (2004), Coronal magnetic field measurements, *Astrophys. J.*, *613*, L177–L180.
Linker, J. A., and Z. Mikić (1995), Disruption of a helmet streamer by photospheric shear, *Astrophys. J.*, *438*, L45–L48.
Linker, J. A., Z. Mikić, D. A. Biesecker, R. J. Forsyth, S. E. Gibson, A. J. Lazarus, A. Lecinski, P. Riley, A. Szabo, and B. J. Thompson (1999), Magnetohydrodynamic modeling of the solar corona during Whole Sun Month, *J. Geophys. Res.*, *104*, 9809–9830.
Lionello, R., J. A. Linker, and Z. Mikić (2001), Including the transition region in models of the large-scale solar corona, *Astrophys. J.*, *546*, 542–551.
Marsch, E. (1991), Kinetic physics of the solar wind plasma, in *Physics of the Inner Heliosphere, 2, Particles, Waves and Turbulence*, edited by R. Schwenn, and E. Marsch, pp. 45–133, Springer, New York.
Ofman, L. (2004), Three-fluid model of the heating and acceleration of the fast solar wind, *J. Geophys. Res.*, *109*, A07102, doi:10.1029/2003JA010221.
Ofman, L., and J. M. Davila (1997), Solar wind acceleration by solitary waves in coronal holes, *Astrophys. J.*, *476*, 357–365.
Ofman, L., and J. M. Davila (1998), Solar wind acceleration by large-amplitude nonlinear waves: Parametric study, *J. Geophys. Res.*, *103*, 23,677–23,690.
Olsen, E. L., and E. Leer (1996), An eight-moment approximation two-fluid model of the solar wind, *J. Geophys. Res.*, *101*, 15,591–15,604.
Pneuman, G. W., and R. A. Kopp (1971), Gas-magnetic field interactions in the solar corona, *Sol. Phys.*, *18*, 258–270.
Robertson, B. J. (1983), Self-consistent Magnetohydrodynamic coronal hole flows, *Sol. Phys.*, *83*, 63–82.
Spitzer, L., Jr. (1962), *Physics of Fully Ionized Gases*, Wiley-Interscience, New York.
Steinolfson, R. S., S. T. Suess, and S. T. Wu (1982), The steady global corona, *Astrophys. J.*, *255*, 730–742.
Stewart, G. A., and S. Bravo (1997), Latitudinal solar wind velocity variations from polar coronal holes: A self-consistent MHD model, *J. Geophys. Res.*, *102*, 11,263–11,272.
Suess, S. T., A.-H. Wang, and S. T. Wu (1996), Volumetric heating in coronal streamers, *J. Geophys. Res.*, *101*, 19,957–19,966.
Suess, S. T., G. A. Gary, and S. F. Nerney (1999a), β in streamers, in *Solar Wind 9*, edited by S. R. Habbal, R. Esser, J. V. Hollweg, and P. A. Isenberg, *AIP Conf. Proc.*, *471*, 247–250.
Suess, S. T., A.-H. Wang, S. T. Wu, G. Poletto, and D. J. McComas (1999b), A two-fluid, MHD coronal model, *J. Geophys. Res.*, *104*, 4697–4708.
Svalgaard, L., T. L. Duvall, and P. H. Scherrer (1978), The strength of the sun's polar fields, *Sol. Phys.*, *58*, 225–239.
Tu, C., C. Zhou, E. Marsch, L. Xia, L. Zhao, J. Wang, and K. Wilhelm (2005), Solar wind origin in coronal funnels, *Science*, *308*, 519–523.
Usmanov, A. V. (1993), A global numerical 3-D MHD model of the solar wind, *Sol. Phys.*, *146*, 377–396.
Usmanov, A. V., and M. L. Goldstein (2003), A tilted-dipole MHD model of the solar corona and solar wind, *J. Geophys. Res.*, *108*(A9), 1354, doi:10.1029/2002JA009777.
Usmanov, A. V., M. L. Goldstein, B. P. Besser, and J. M. Fritzer (2000), A global MHD solar wind model with WKB Alfvén waves: Comparison with Ulysses data, *J. Geophys. Res.*, *105*, 12,675–12,695.
Vásquez, A. M., A. A. van Ballegooijen, and J. C. Raymond (2003), The effect of proton temperature anisotropy on the solar minimum corona and wind, *Astrophys. J.*, *598*, 1361–1374.
Wang, A.-H., S. T. Wu, S. T. Suess, and G. Poletto (1993), A two-dimensional MHD global coronal model - Steady-state streamers, *Sol. Phys.*, *147*, 55–71.
Wang, A.-H., S. T. Wu, S. T. Suess, and G. Poletto (1998), Global model of the corona with heat and momentum addition, *J. Geophys. Res.*, *103*, 1913–1922.
Washimi, H., T. Ogino, and Y. Yoshino (1987), Two-dimensional structure of the solar wind near the Sun, *Geophys. Res. Lett.*, *14*, 487–490.
Yeh, T., and G. W. Pneuman (1977), A sheet-current approach to coronal-interplanetary modeling, *Sol. Phys.*, *54*, 419–430.

S. R. Habbal, Institute for Astronomy, University of Hawaii, 2680 Woodlawn Drive, Honolulu, HI 96822, USA.
B. Li and X. Li, Institute of Mathematical and Physical Sciences, University of Wales Aberystwyth, Aberystwyth, SY23 3BZ, UK. (bbl@aber.ac.uk)
C. Mountford, Department of Computer Science, University of York, Heslington, York YO10 5DD, UK.